

Origin of ferroelectric-like orthorhombic phase in oxygen-deficient HfO_{2-y} nanoparticles

E.A. Eliseev^{1*}, I.V. Kondakova¹, Yu.O. Zagorodniy¹, H.V. Shevliakova², O.V. Leshchenko¹, V.N. Pavlikov¹, L.P. Yurchenko¹, M.V. Karpets¹, and A.N. Morozovska^{3**}

¹*I. Frantsevich Institute for Problems in Materials Science, National Academy of Sciences of Ukraine Kyiv, Ukraine*

²*Department of Microelectronics, National Technical University of Ukraine*

“Igor Sikorsky Kyiv Polytechnic Institute”, Kyiv, Ukraine

³*Institute of Physics, National Academy of Sciences of Ukraine, Kyiv, Ukraine*

Corresponding author e-mail: eugene.a.eliseev@gmail.com*; anna.n.morozovska@gmail.com**

Abstract. In this work, the relationship between the crystalline structure symmetry, concentration of point defects and possible appearance of ferroelectric-like polarization in HfO_{2-y} nanoparticles was established. The X-ray diffraction and electron paramagnetic resonance analyses revealed the formation of ferroelectric-like orthorhombic phase in oxygen-deficient HfO_{2-y} nanoparticles (pure and doped with rare-earth element yttrium ones). Density functional theory (DFT) calculations showed that small HfO_2 nanoparticles may become polar, especially in the presence of impurity atoms and/or oxygen vacancies. To explain the experimental results, we modified the effective Landau–Ginzburg–Devonshire (LGD) model using the parameterization approach, focusing on the Landau expansion coefficients associated with polar and antipolar orderings, which agrees with the performed DFT calculations. The effective LGD model may be useful for developing silicon-compatible ferroelectric nanomaterials based on $\text{Hf}_x\text{Zr}_{1-x}\text{O}_{2-y}$.

Keywords: nanoparticles, hafnium oxide, oxygen vacancies, rare-earth element doping, ferroelectric-like polar phase, silicon-compatible ferroelectric nanomaterials.

<https://doi.org/10.15407/spqeo28.02.134>

PACS 61.05.cp, 73.22.-f, 76.30.-v, 77.80.B-

Manuscript received 06.12.24; revised version received 12.04.25; accepted for publication 11.06.25; published online 26.06.25.

1. Introduction

The discovery of ferroelectric and antiferroelectric properties in thin films of lead-free hafnium (HfO_2) and zirconium (ZrO_2) oxides has opened them for next-generation Si-compatible ferroelectric memory elements such as ferroelectric random-access memories (FeRAMs) and field-effect transistors (FETs) [1, 2]. However, comprehensive understanding of the crucial interplay between stoichiometry, oxygen vacancy concentration, nanoparticle size, and surface effects in nanosized $\text{Hf}_x\text{Zr}_{1-x}\text{O}_{2-y}$ still remains elusive [3].

Bulk HfO_2 and ZrO_2 , characterized as high- k dielectrics, lack inherent ferroelectric properties across a wide range of standard temperatures and pressures [4, 5]. This behavior dramatically changes when the materials under consideration are scaled down to nanoscale and complex interactions and structural transitions come into play. One key factor influencing the observed ferroelectric properties in $\text{Hf}_x\text{Zr}_{1-x}\text{O}_2$ films is the

presence of a polar orthorhombic phase. However, this phase is metastable compared to the bulk monoclinic phase, which leads to challenges with ferroelectric phase stability. Moreover, the properties of such thin films are highly sensitive to various factors, including substrate material, annealing conditions, deposition method, film thickness, and dopant concentrations [6–8]. Depending on the interplay of these factors, the value of x in $\text{Hf}_{1-x}\text{Zr}_x\text{O}_2$ films can range from 0 to 1, ultimately dictating whether the material would exhibit dielectric, ferroelectric, or antiferroelectric behavior [9, 10].

Extensive theoretical [11–13] and experimental [14–16] investigations, as highlighted in our previous studies [29–31], underscore the critical role of surface and grain boundary energy, alongside with oxygen vacancy concentration, on optimizing these materials for practical applications in advanced FeRAM and FET technologies. However, further research and optimization efforts are required to fully uncover the potential of $\text{Hf}_x\text{Zr}_{1-x}\text{O}_{2-y}$ binary oxide nanoparticles (see Table 1).

Table 1. Properties of $\text{Hf}_x\text{Zr}_{1-x}\text{O}_{2-y}$ nanoparticles and thin films (for comparison).

Material	Doping	Geometry	Size/thickness (nm)	Symmetry group(s)	Ferroelectric properties	Synthesis method	Ref.
$\text{Hf}_x\text{Zr}_{1-x}\text{O}_2$	none	Particles of faceted shape	5.5, 4.3, 3.6	tetragonal or cubic	n/m	sol-gel	17
HfO_2	none	particle	10 – 15	monoclinic phase ($P2_1/c$)	n/m	auto-igniting combustion	18
HfO_2	none	spherical particles	8.79, 7.16, 6.78	monoclinic	n/m	precipitation method	19
HfO_2	none	particle	4 – 120	tetragonal and monoclinic	n/m	hydrothermal route	20
HfO_2	none	particle	61 – 80	n/m	low loss dielectric composite	US Research Nanomaterials, Inc.	21
HfO_2	none	particle	60 – 90	monoclinic	n/m	hydrothermal synthesis	22
HfO_2	co-doped with Dy and Sm	particle	10 – 31	monoclinic and cubic phases	n/m	Pechini type sol-gel method	23
$\text{Hf}_x\text{Zr}_{1-x}\text{O}_{2-y}$	O-vacancies	particle	n/m	m o + m	possible (from X-ray diffraction) Yes (theory)	organo-nitrate; pyrogenic	24
HfO_2	either Eu^{3+} or Nb^{5+} doping	particle	17 – 47	monoclinic + small amount of tetragonal phase	n/m	sol-gel and combustion synthesis	25
$\text{Hf}_{0.5}\text{Zr}_{0.5}\text{O}_2$	none	particles of spindle-like or spherical shape	200 – 50 3 – 4	orthorhombic $Pca2_1$ $Pbca$, $Pbcm$	possible from XRD	hydrothermal synthesis from HfCl_4 and ZrCl_4	26
HfO_2	Si-, Al-, Gd-doped	film	10 nm and 40 nm thick	Orthorhombic ($Pca2_1$)	polarization hysteresis in electric field	atomic layer deposition (ALD)	27
$\text{Hf}_{0.5}\text{Zr}_{0.5}\text{O}_2$	none O-deficient (air, high-vacuum, Ar)	film	17 nm	orthorhombic /tetragonal	Yes (local piezoresponse hysteresis loop)	plasma-enhanced ALD	28

This work aims to bridge this gap in the knowledge by investigating structural and polar properties of $\text{Hf}_x\text{Zr}_{1-x}\text{O}_{2-y}$ materials using the Landau–Ginzburg–Devonshire (LGD) model [29–31] in conjunction with DFT calculations. This allows us to determine the “effective” Landau expansion coefficients for polar (FE) and antipolar (AFE) orderings in hafnia-based compounds. To verify the effectiveness of the LGD model, we explain the X-ray diffraction (XRD) and electron paramagnetic resonance (EPR) data for oxygen-deficient HfO_{2-y} nanoparticles to determine their phase composition, as well as for the nanoparticles prepared under varying annealing conditions (pure and yttrium-doped ones) and explain the formation of the ferroelectric-like orthorhombic phase in them.

2. Theoretical description

A. “Effective” Landau–Ginzburg–Devonshire model

A spatial-temporal evolution of polarization in nanosized $\text{Hf}_x\text{Zr}_{1-x}\text{O}_{2-y}$ is further analyzed using a combined approach. This approach includes elements of the Kittel-type model [32], incorporating both polar and antipolar modes [33–35], with the theoretical framework of the LGD approach [29–31]. Within this framework, the free energy functional F is expressed as the sum of several key terms [29–31]:

$$F = F_{\text{bulk}} + F_{\text{grad}} + F_{\text{el}} + F_S. \quad (1)$$

The first term represents the bulk free energy in form of an expansion, which includes second and fourth powers

Table 2. Landau–Ginsburg–Devonshire parameters of $\text{Hf}_x\text{Zr}_{1-x}\text{O}_2$ films*.

x	phase	$P_r(x)$, C/m^2	$P_{c1,2}(x)$, C/m^2	$\tilde{\chi}(x)$	$a_P(x) \times 10^9$, m/F	$a_A(x) \times 10^9$, m/F	$b_P \approx b_A \times 10^{10}$, $\text{V} \cdot \text{m}^5/\text{C}^3$	$\eta(x) \times 10^{10}$, $\text{V} \cdot \text{m}^5/\text{C}^3$
0	PE	0	N/A	35	3.227	N/P	N/P	N/P
0.2	AFE	0	0.22, 0.17	40	0.812	-0.936	0.9	1.93
0.3	AFE	0	0.22, 0.15	50	0.010	-1.190	1.3	2.458
0.4	AFE	0	0.18, 0.11	48	-0.104	-0.937	1.1	2.888
0.50	FE	0.195	N/A	95	-0.594	N/P	1.563	N/P
0.57	FE	0.173	N/A	76	-0.743	N/P	2.483	N/P
0.70	FE	0.038	N/A	400	-0.141	N/P	10.039	N/P
0.81	PE	0.025	N/A	31	3.643	N/P	N/P	N/P
1.00	PE	0	N/A	19	5.944	N/P	N/P	N/P
h	films with thickness $h = 9.2$ nm							

*The content of Table 2 is licensed under a Creative Commons Attribution (CC BY) license (<https://creativecommons.org/licenses/by/4.0/>) in Supplementary Information to Ref. [<https://doi.org/10.1063/5.0209123>]

of both the polar (P_f) and antipolar (A_f) order parameters as follows:

$$F_{bulk} = \int_{V_f} d^3r \left(\frac{a_P}{2} P_f^2 + \frac{b_P}{4} P_f^4 + \frac{\eta}{2} P_f^2 A_f^2 + \frac{a_A}{2} A_f^2 + \frac{b_A}{4} A_f^4 \right). \quad (2a)$$

Here, V_f is the volume of a HfO_{2-y} nanoparticle. The next terms in expression (1) account for the energy contribution due to gradients of polarization (F_{grad}), the electrostatic energy (F_{el}), and the surface energy (F_S) as listed in [29–31].

It is important to consider how the LGD expansion coefficients depend on various factors, which in turn may be influenced by temperature, size, elastic stresses and/or strains. For classical ferroelectric films with a pronounced temperature-dependent and strain-dependent soft mode, the coefficients a_P and a_A exhibit a linear relationship with both temperature and strain (as shown in [36, 37]).

Spatial-temporal evolution of P_f and A_f is determined by solving the following coupled time-dependent LGD type Euler–Lagrange equations, derived by minimizing the system free energy F :

$$\Gamma_P \frac{\partial P_f}{\partial t} + a_P P_f + b_P P_f^3 + \eta A_f^2 P_f - g \Delta P_f = E_f, \quad (3a)$$

$$\Gamma_A \frac{\partial A_f}{\partial t} + a_A A_f + b_A A_f^3 + \eta P_f^2 A_f - g \Delta A_f = 0, \quad (3b)$$

Here, Γ_P and Γ_A are the Landau–Khalatnikov relaxation coefficients, and g is a positive gradient coefficient written in an isotropic approximation, respectively. The relaxation times of P_f and A_f are $\tau_P = \Gamma_P/|a_P|$ and $\tau_A = \Gamma_A/|a_A|$, respectively. The corresponding boundary conditions for (3) are of the third kind [38]:

$$\left(P_f + \Lambda_P \frac{\partial P_f}{\partial n} \right) \Big|_S = 0, \quad \left(A_f + \Lambda_A \frac{\partial A_f}{\partial n} \right) \Big|_S = 0, \quad (4)$$

Here, $\Lambda_P = \frac{g}{C_P}$ and $\Lambda_A = \frac{g}{C_A}$ are the extrapolation lengths, which physical range is 0.5...5 nm [39], and S is the HfO_{2-y} nanoparticle surface, respectively.

Examples of how the effective LGD model works quantitatively are presented in [29–31]. In those publications, polarization hysteresis loops, measured experimentally in $\text{Hf}_x\text{Zr}_{1-x}\text{O}_2$ thin films by Park *et al.*, are shown. The LGD-model parameters, determined in [29–31] by fitting the experimental results from Park *et al.* [9] are listed in the last four columns of Table 2.

B. Density Functional Theory calculations

Calculations were made using density functional theory, which allowed us to obtain the parameters of the ground state structure by minimizing the total energy functional. It should be noticed that the functional is not exactly known, and the result depends on its model form. The calculations were performed using the full-electron package FPLO (full potential local orbital) for the local density approximation (LDA) and generalized gradient approximation (GGA) functionals. The FPLO basis was used. 12-atom hafnium oxide supercells containing crystalline phases of different symmetries were simulated with a $6 \times 6 \times 6$ grid of k -points in the Brillouin zone. The equilibrium lattice parameters were found and compared with the experimental data and the respective values determined using other calculation packages. For both functionals, we confirmed that the crystal structure with monoclinic symmetry in bulk HfO_2 has the lowest ground state energy. At the same time, the difference between the energies of the polar orthorhombic phase (shown in Fig. 1b) and monoclinic phase (shown in Fig. 1a)

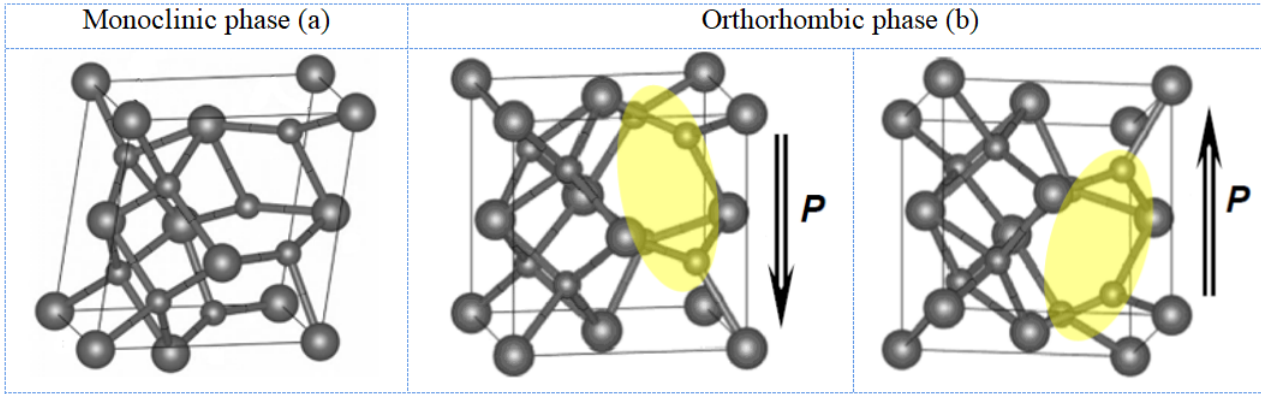


Fig. 1. HfO₂ structure with nonpolar monoclinic symmetry (a) and polar orthorhombic symmetry (b). The polarization of the orthorhombic phase can be visualized as a shift of four oxygen atoms (shown by the yellow area) along *z*-direction. Adapted from [40].

calculated by the LDA and GGA approximations turns out to be smaller (by ~20 meV/f.u.) than that calculated by other methods.

The accuracy of the DFT energy calculations becomes a significant factor in determining the type of defects (dopants or vacancies) that promote formation of a ferroelectric phase in HfO₂ and define the mechanisms that stabilize the polar phase under action of finite electric fields. Thus, the DFT calculations reveal that small HfO₂ nanoparticles may become polar, especially in the presence of impurity atoms and/or oxygen vacancies.

A. X-ray diffraction spectra of oxygen-deficient HfO_{2-y} nanoparticles

To verify the model, we prepared several sample groups of stoichiometric HfO₂, oxygen-deficient HfO_{2-y} and HfO_{2-y} nanoparticles doped with Y. Namely:

- Sample group 1 annealed at 700 °C for 6 hours (or more) in air,
- Sample group 2 annealed at 600 °C for 6 hours in air + 3.8 mol.% of Y₂O₃,
- Sample group 3 annealed at 500 °C for 6 hours in CO + CO₂.

This diverse approach yielded the samples with distinct color variations, reflecting differences in their oxygen vacancy concentrations. Namely, for the samples from 1 to 3, the color changed from white to dark grey.

The average size of the nanoparticles (20 nm) was determined by transmission electron microscopy.

X-ray diffraction (XRD) analysis using an XRD-6000 diffractometer with a Cu-Kα1 radiation source (2θ = 15...70°) and the database of the International Committee for Powder Diffraction Standards (JCPDS PDF-2) was applied for identifying crystallographic phases of the HfO₂ nanoparticles. As a result, we confirmed the coexistence of both monoclinic and ferroelectric-like orthorhombic phases inside the oxygen-deficient nanoparticles. Namely, significant amounts of these phases were found in the sample groups 2 and 3 (see Table 3). Notably, the relative abundance of each phase exhibited a demonstrably shifting pattern based on the specific annealing protocol employed, highlighting the sensitivity of the phase composition to the processing parameters.

The XRD analysis revealed a progressive shift in the sample phases with changing the annealing conditions. The sample group 1 has the pure monoclinic phase (“m”) as should be the case for a stoichiometric HfO₂ nanopowder. The fraction of the non-ferroelectric monoclinic phase (“m”) decreased from 100% (for the sample group 1) to 13.24% (for the sample group 3), while the content of the ferroelectric-like orthorhombic phase (“o”) increased from 0% (for the sample group 1) to 86.76% (for the sample group 3). The progressive change in the phase composition, namely increase of the content of the ferroelectric-like orthorhombic phases, is attributed to the

Table 3. XRD studies of HfO_{2-y} nanopowder sample groups.

Sample group No.	Phase	Mass fraction, %	Scattering region size, nm	Lattice parameters		
				<i>a</i> , Å	<i>b</i> , Å	<i>c</i> , Å
1	m	100	13	5.1220	5.1603	5.3025
2	m	16.85	11	5.1408	5.1771	5.4113
	o	83.15	7	10.1180	5.1353	5.1583
3	m	13.24	12	5.1250	5.1580	5.3048
	o	86.76	8	10.1089	5.2076	5.1202

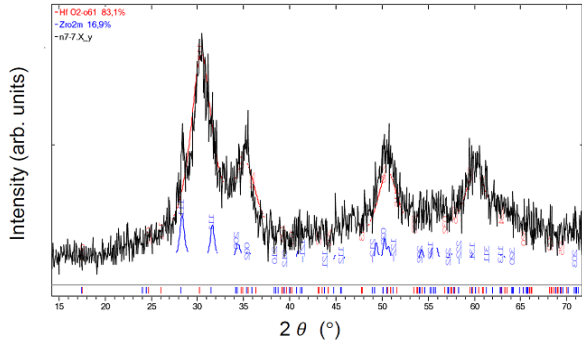


Fig. 2. XRD spectra of oxygen-deficient HfO_{2-y} nanopowders annealed at 600 °C for 6 hours in air at the presence of 3.8 mol.% of Y_2O_3 .

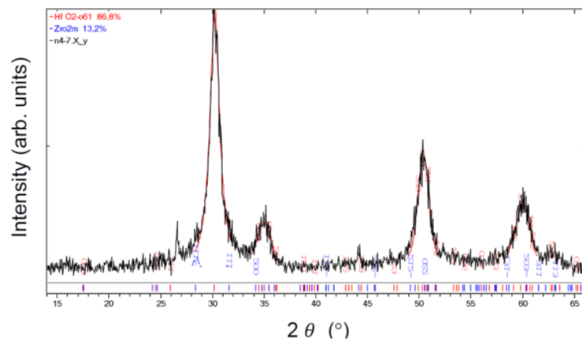


Fig. 3. XRD spectra of oxygen-deficient HfO_{2-y} nanopowders annealed at 500 °C for 6 hours in $\text{CO} + \text{CO}_2$ atmosphere.

the rise in the oxygen vacancy concentration induced by specific annealing conditions and/or rare-earth doping. The corresponding XRD spectra of the oxygen-deficient HfO_{2-y} nanopowders are shown in Figs. 2 and 3, respectively.

This comprehensive dataset, along with the sizes of the coherent scattering regions, forms the foundation for subsequent verification of the proposed effective LGD model.

B. EPR spectra of oxygen-deficient HfO_{2-y} nanoparticles

EPR measurements were carried out on an X-band Bruker Elexsys E580 spectrometer operating at a frequency of 9.8 GHz at room temperature. The EPR spectra of the HfO_{2-y} and $\text{HfO}_2 + 3.8$ mol.% of Y_2O_3 nanoparticles are presented in Fig. 4. The Y^{3+} and Hf^{4+} ions have closed electron shells and do not contribute to the observed spectra. Therefore, the spectral line may be due to impurities present in the studied samples, charged oxygen vacancies, or Y^{2+} or Hf^{3+} cations that have lowered their valence state due to the formation of oxygen vacancies.

The sharp intense line in Fig. 4a corresponds to organic radicals present in the sample annealed in a $\text{CO} + \text{CO}_2$ atmosphere, while the weak signal with $g_{\text{eff}} \sim 4.25$ is characteristic of Fe^{3+} impurities. Much more interesting is the line with $g_{\text{eff}} \sim 1.98$ shown in the inset in

Fig. 4a. According to [41], this line may be attributed to a Hf^{3+} ion associated with an oxygen vacancy. The sharp, well-shaped signal apparently corresponds to Hf in the bulk of the sample, which is not affected by defects present on the nanoparticle surface. On the other hand, Hf^{3+} located in the near-surface layer should give a broad line due to the distribution of the parameters that define the EPR line shape. Therefore, the line with $g_{\text{eff}} \sim 2.43$ may correspond to a large near-surface layer abundant in oxygen vacancies and Hf^{3+} cations.

The entire spectrum shown in Fig. 4b has a very weak intensity. Its true magnitude can be estimated from the signal associated with the Fe^{3+} impurity, whose intensity is close to the appropriate signal in Fig. 4a. The broad line centered at $g_{\text{eff}} \sim 2.2$ can be described by a superposition of at least two wide lines. This line may be associated with the presence of an Y^{2+} ion [42], the EPR parameters of which are affected by surface defects. However, there is a significant difference from the values of the EPR parameters given in the mentioned work. Moreover, annealing in an oxygen atmosphere makes the formation of Y^{2+} ions very unlikely. Thus, the nature of this line in the EPR spectrum requires further detailed study.

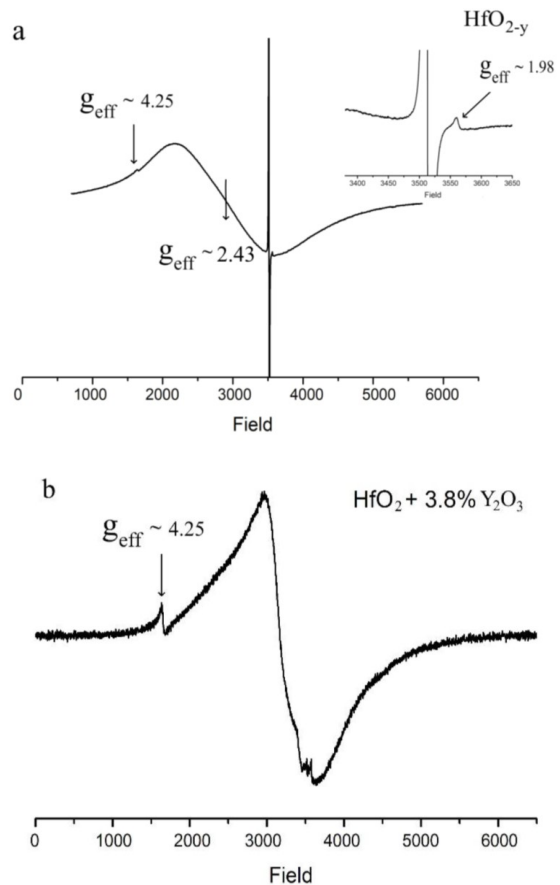


Fig. 4. EPR spectra of oxygen-deficient HfO_{2-y} nanopowders annealed at 500 °C for 6 hours in $\text{CO} + \text{CO}_2$ atmosphere (a) and $\text{HfO}_2 + 3.8$ mol.% of Y_2O_3 nanoparticles annealed at 600 °C for 6 hours in air (b).

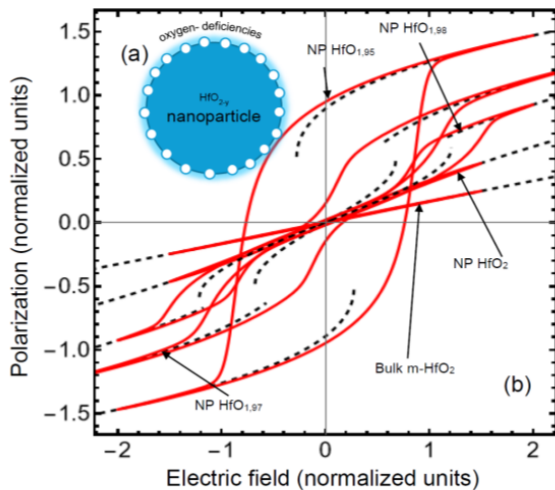


Fig. 5. (a) Radial cross-section of an oxygen-deficient HfO_{2-y} nanoparticle. (b) Polarization-field dependences (hysteresis loops) calculated using the effective LGD model for the stoichiometric HfO_2 bulk, 20-nm size stoichiometric HfO_2 nanoparticles and HfO_{2-y} nanoparticles with different concentrations of oxygen vacancies near the surface: $y = 2\%$, 3% and 5% . The dielectric-type, paraelectric-type, antiferroelectric-type and ferroelectric-type loops are shown. Black dotted curves show the equilibrium polarization-field dependences. Red solid curves show the dynamic polarization-field hysteresis loops.

4. Effective LGD model for oxygen-deficient HfO_{2-y} nanoparticles

Using the phase fractions and coherent scattering region sizes obtained from XRD (Table 3), we employ the effective LGD model to simulate polar and dielectric properties of stoichiometric and oxygen-deficient HfO_2 nanoparticles. The model incorporates a vacancy concentration gradient, mimicking the presumed distribution, as shown in Fig. 5a.

These vacancies act as elastic dipoles, influencing the material stability. The calculated polarization-field hysteresis loops (shown in Fig. 5b) reveal a progressive transition from dielectric-like to antiferroelectric and ferroelectric characteristics with increasing the vacancy concentration, aligning well with the XRD findings.

5. Conclusions

The obtained results indicate strong correlation between the crystalline structure symmetry, concentration of point defects and possible appearance of ferroelectric-like polarization in HfO_{2-y} nanoparticles. Notably, the XRD and EPR analysis revealed the formation of the ferroelectric-like orthorhombic phase in the oxygen-deficient HfO_{2-y} nanoparticles (both in pure and doped with rare-earth element yttrium ones). The DFT calculations also showed that small HfO_2 nanoparticles may become polar, especially in the presence of impurity atoms and/or oxygen vacancies.

To explain the experimental results, we have modified the effective LGD model [29–31] using a tailored parameterization approach, specifically focusing on the

Landau expansion coefficients associated with polar and antipolar orderings, which agrees with the performed DFT calculations. The effective LGD model can be useful for developing novel-generation silicon-compatible ferroelectric nanomaterials based on $\text{Hf}_x\text{Zr}_{1-x}\text{O}_{2-y}$.

The combined experimental and theoretical approach presented in this work has potential for the field of nanotechnology and materials science.

Acknowledgment

The work of E.A.E., I.V.K., Y.O.Z. and L.P.Y. is funded by the National Research Foundation of Ukraine (project “Silicon-compatible ferroelectric nanocomposites for electronics and sensors”, grant No. 2023.03/0127). The work of A.N.M. is funded by the National Research Foundation of Ukraine (project “Manyfold-degenerated metastable states of spontaneous polarization in nanoferroics: theory, experiment and perspectives for digital nanoelectronics”, grant N 2023.03/0132) and Horizon Europe Framework Programme (HORIZON-TMA-MSCA-SE), project № 101131229.

References

1. Mikolajick T., Slesazek S., Mulaosmanovic H. *et al.* Next generation ferroelectric materials for semiconductor process integration and their applications. *J. Appl. Phys.* 2021. **129**. P. 100901. <https://doi.org/10.1063/5.0037617>.
2. Kim K.-H., Karpov I., Olsson R.H. III, Jariwala D. Wurtzite and fluorite ferroelectric materials for electronic memory. *Nat. Nanotechnol.* 2023. **18**. P. 422. <https://doi.org/10.1038/s41565-023-01361-y>.
3. Yang W., Yu C., Li H. *et al.* Ferroelectricity of hafnium oxide-based materials: Current statuses and future prospects from physical mechanisms to device applications. *J. Semicond.* 2023. **44**. P. 053101. <https://doi.org/10.1088/1674-4926/44/5/053101>.
4. Kourouklis G.A., Liarokapis E. Pressure and temperature dependence of the Raman spectra of zirconia and hafnia. *J. Am. Ceram. Soc.* 1991. **74**. P. 520. <https://doi.org/10.1111/j.1151-2916.1991.tb04054.x>.
5. Ishigame M., Sakurai T. Temperature dependence of the Raman spectra of ZrO_2 . *J. Am. Ceram. Soc.* 1977. **60**. P. 367. <https://doi.org/10.1111/j.1151-2916.1977.tb15561.x>.
6. Boscke T.S., Teichert S., Brauhaus D. *et al.* Phase transitions in ferroelectric silicon doped hafnium oxide. *Appl. Phys. Lett.* 2011. **99**. P. 112904. <https://doi.org/10.1063/1.3636434>.
7. Yun Y., Buragohain P., Li M. *et al.* Intrinsic ferroelectricity in Y-doped HfO_2 thin films. *Nat. Mater.* 2022. **21**. P. 903. <https://doi.org/10.1038/s41563-022-01282-6>.
8. Delodovici F., Barone P., Picozzi S. Finite-size effects on ferroelectricity in rhombohedral HfO_2 . *Phys. Rev. B.* 2022. **106**. P. 115438. <https://doi.org/10.1103/PhysRevB.106.115438>.
9. Park M.H., Lee Y.H., Kim H.J. *et al.* Surface and grain boundary energy as the key enabler of ferroelectricity in nanoscale hafnia-zirconia: a comparison

- of model and experiment. *Nanoscale*. 2017. **9**. P. 9973. <https://doi.org/10.1039/C7NR02121F>.
10. Lee D.H., Lee Y., Yang K. *et al.* Domains and domain dynamics in fluorite-structured ferroelectrics. *Appl. Phys. Rev.* 2021. **8**. P. 021312. <https://doi.org/10.1063/5.0047977>.
 11. Ma L.-Y., Liu S. Structural polymorphism kinetics promoted by charged oxygen vacancies in HfO₂. *Phys. Rev. Lett.* 2023. **130**. P. 096801. <https://doi.org/10.1103/PhysRevLett.130.096801>.
 12. Glinchuk M.D., Morozovska A.N., Lukowiak A. *et al.* Possible electrochemical origin of ferroelectricity in HfO₂ thin films. *J. Alloys Compd.* 2020. **830**. P. 153628. <https://doi.org/10.1016/j.jallcom.2019.153628>.
 13. Kang S., Jang W.-S., Morozovska A.N. *et al.* Highly enhanced ferroelectricity in HfO₂-based ferroelectric thin film by light ion bombardment. *Science*. 2022. **376**. P. 731–738. <https://doi.org/10.1126/science.abk3195>.
 14. Yang W., Yu C., Li H. *et al.* Ferroelectricity of hafnium oxide based materials: Current statuses and future prospects from physical mechanisms to device applications. *J. Semicond.* 2023. **44**. P. 1–45. <https://doi.org/10.1088/1674-4926/44/5/053101>.
 15. Park M.H., Chung C.-C., Schenk T. *et al.* Effect of annealing ferroelectric HfO₂ thin films: in situ, high temperature X-ray diffraction. *Adv. Electron. Mater.* 2018. **4**. P. 1800091. <https://doi.org/10.1002/aelm.201800091>.
 16. Kelley K.P., Morozovska A.N., Eliseev E.A. *et al.* Ferroelectricity in Hafnia controlled via surface electrochemical state. *Nat. Mater.* 2023. **22**. P. 1144. <https://doi.org/10.1038/s41563-023-01619-9>.
 17. Tang J., Fabbri J., Robinson R.D. *et al.* Solid-solution nanoparticles: Use of a nonhydrolytic sol-gel synthesis to prepare HfO₂ and Hf_xZr_{1-x}O₂ nanocrystals. *Chem. Mater.* 2004. **16**. P. 1336. <https://doi.org/10.1021/cm049945w>.
 18. Kumar H.P., Vidya S., Kumar S.S. *et al.* Optical properties of nanocrystalline HfO₂ synthesized by an auto-igniting combustion synthesis. *J. Asian Ceram. Soc.* 2015. **3**. P. 64–69. <http://doi.org/10.1016/j.jascer.2014.10.009>.
 19. Jayaraman V., Bhavesh G., Chinnathambi S. *et al.* Synthesis and characterization of hafnium oxide nanoparticles for bio-safety. *Mater. Express*. 2014. **4**. P. 375. <https://doi.org/10.1166/mex.2014.1190>.
 20. Wan Y., Zhou X. Formation mechanism of hafnium oxide nanoparticles by a hydrothermal route. *RSC Adv.* 2017. **7**. P. 7763. <https://doi.org/10.1039/C6RA26663K>.
 21. Ren L., Yang L., Zhang S. *et al.* Largely enhanced dielectric properties of polymer composites with HfO₂ nanoparticles for high-temperature film capacitors. *Compos. Sci. Technol.* 2021. **201**. P. 108528. <https://doi.org/10.1016/j.compscitech.2020.108528>.
 22. McGinnity T.L., Sokolova V., Prymak O. *et al.* Colloidal stability, cytotoxicity, and cellular uptake of HfO₂ nanoparticles. *J. Biomed. Mater. Res. B: Appl. Biomater.* 2021. **109**. P. 1407. <https://doi.org/10.1002/jbmb.b.34800>.
 23. Kumar S., Dehury T., Rath C. Stabilization of cubic phase at room temperature and photoluminescence properties of Dy and Sm Co-doped HfO₂ nanoparticles. *ECS J. Solid State Sci. Technol.* 2021. **10**. P. 081009. <https://doi.org/10.1149/2162-8777/ac1c54>.
 24. Eliseev E.A., Zagorodniy Yu.O., Pavlikov V.N. *et al.* Phase diagrams and polarization reversal in nanosized Hf_xZr_{1-x}O_{2-y}. *AIP Adv.* 2024. **14**. P. 055224. <https://doi.org/10.1063/5.0209123>.
 25. Laganovska K., Vitola V., Einbergs E. *et al.* Impact of europium and niobium doping on hafnium oxide (HfO₂): Comparative analysis of sol-gel and combustion synthesis methods. *Ceramics*. 2024. **7**. P. 15–28. <https://doi.org/10.3390/ceramics7010002>.
 26. Fujimoto K., Sato Y., Fuchikami Y. *et al.* Orthorhombic-like atomic arrangement in hafnium-oxide-based nanoparticles. *J. Am. Ceram. Soc.* 2022. **105**. P. 2823–2831. <https://doi.org/10.1111/jace.18242>.
 27. Park M.H., Chung C.-C., Schenk T. *et al.* Effect of Annealing ferroelectric HfO₂ thin films: in situ, high temperature X-ray diffraction. *Adv. Electron. Mater.* 2018. **4**. P. 1800091. <https://doi.org/10.1002/aelm.201800091>.
 28. Kelley K.P., Morozovska A.N., Eliseev E.A. *et al.* Ferroelectricity in hafnia controlled via surface electrochemical state. *Nat. Mater.* 2023. **22**. P. 1144. <https://doi.org/10.1038/s41563-023-01619-9>.
 29. Morozovska A.N., Strikha M.V., Kelley K.P. *et al.* Effective Landau-type model of a Hf_xZr_{1-x}O_{2-y} graphene nanostructure. *Phys. Rev. Appl.* 2023. **20**. P. 054007. <https://doi.org/10.1103/PhysRevApplied.20.054007>.
 30. Eliseev E.A., Zagorodniy Y.O., Pavlikov V.N. *et al.* Phase diagrams and polarization reversal in nanosized Hf_xZr_{1-x}O_{2-y}. *AIP Adv.* 2024. **14**. P. 055224. <https://doi.org/10.1063/5.0209123>.
 31. Eliseev E.A., Kalinin S.V., Morozovska A.N. Ferroionic states and domains morphology in Hf_xZr_{1-x}O₂ nanoparticles. *J. Appl. Phys.* 2025. **137**. P. 034103. <https://doi.org/10.1063/5.0243067>.
 32. Blinc R., Zeks B. *Soft Mode in Ferroelectrics and Antiferroelectrics*. North-Holland Publ. Company, Amsterdam, Oxford, 1974.
 33. Tagantsev A.K., Vaideeswaran K., Vakhrushev S.B. *et al.* The origin of antiferroelectricity in PbZrO₃. *Nature Commun.* 2013. **4**. P. 2229. <https://doi.org/10.1038/ncomms3229>.
 34. Rabe K.M. *Antiferroelectricity in Oxides: A Reexamination*. In: *Functional Metal Oxides*. John Wiley & Sons, Ltd. P. 221–244. <https://doi.org/10.1002/9783527654864.ch7>.
 35. Hlinka J., Ostapchuk T., Buixaderas E. *et al.* Multiple soft-mode vibrations of lead zirconate. *Phys. Rev. Lett.* 2014. **112**. P. 197601. <https://doi.org/10.1103/PhysRevLett.112.197601>.

36. Tagantsev A., Cross L.E., Fousek J. *Domains in Ferroic Crystals and Thin Films*. Springer: N. Y., 2010. <https://doi.org/10.1007/978-1-4419-1417-0>.
37. Kvasov A., Tagantsev A. Role of high-order electromechanical coupling terms in thermodynamics of ferroelectric thin films. *Phys. Rev. B*. 2013. **87**. P. 184101. <https://doi.org/10.1103/PhysRevB.87.184101>.
38. Kretschmer R. Binder K. Surface effects on phase transitions in ferroelectrics and dipolar magnets. *Phys. Rev. B*. 1979. **20**. P. 1065. <https://doi.org/10.1103/PhysRevB.20.1065>.
39. Jia C.-L., Nagarajan V., He J.-Q. *et al.* Unit-cell scale mapping of ferroelectricity and tetragonality in epitaxial ultrathin ferroelectric films. *Nat. Mater.* 2007. **6**. P. 64. <https://doi.org/10.1038/nmat1808>.
40. Materlik R., Kunneth C., Kersch A. The origin of ferroelectricity in $\text{Hf}_{1-x}\text{Zr}_x\text{O}_2$: A computational investigation and a surface energy model. *J. Appl. Phys.* 2015. **11**. P. 134109. <http://doi.org/10.1063/1.4916707>.
41. Wright S., Barklie R.C. EPR characterization of defects in m-HfO₂. *J. Mater. Sci.: Mater. Electron.* 2007. **18**. P. 743–746. <http://doi.org/10.1007/s10854-007-9119-6>.
42. Fang M., Lee D.S., Ziller J.W. *et al.* Synthesis of the $(\text{N}_2)^{3-}$ radical from Y^{2+} and its protonolysis reactivity to form $(\text{N}_2\text{H}_2)^{2-}$ via the $\text{Y}[\text{N}(\text{SiMe}_3)_2]_3/\text{K}_2\text{C}_8$ reduction system. *J. Am. Chem. Soc.* 2011. **133**, No 11. P. 3784–3787. <https://doi.org/10.1021/ja1116827>.

Authors and CV



Eugene Anatolievich Eliseev, born in 1977. PhD in Solid State Physics (2003), Doctor of Sciences in Solid State Physics (2009), Senior Researcher (2015), Head of the Department of Functional Oxide Materials, Department of Solid State Electronics, Institute of Physics. Author of more than 350 scientific publications. The area of his scientific interests is theory of ferroics and phase diagrams, mixed ionic-electronic conductors and related materials. <https://orcid.org/0000-0001-8124-8857>



Anna Nikolaevna Morozovska, born in 1977, PhD in Optics and Laser Physics (2004), Doctor of Sciences in Solid State Physics (2009), Professor in Physics and Astronomy (2023), Leading Scientific Researcher at the Department of Physics of Magnetic Phenomena at the Institute of Physics. Author of more than 400 scientific publications. The area of her scientific interests is theory of ferroics and multiferroics, mixed ionic-electronic conductors and related materials. <https://orcid.org/0000-0002-8505-458X>

Authors' contributions

The research idea belongs to E.A.E., A.N.M. and Y.O.Z. E.A.E. wrote the codes, performed numerical calculations and compared the calculation results to the experiments. I.V.K. performed the DFT calculations. Y.O.Z. performed the EPR measurements. O.V.L., V.N.P. and L.P.Y. prepared the samples. M.V.K. performed the XRD measurements. A.N.M. and H.V.S. wrote the manuscript draft. All the co-authors discussed the obtained results.

Походження сегнетоелектричної орторомбічної фази в наночастинках HfO_{2-y} з дефіцитом кисню

Є.А. Єлісеєв, І.В. Кондакова, Ю.О. Загородній, Г.В. Шевлякова, О.В. Лещенко, В.Н. Павліков, Л.П. Юрченко, М.В. Карпець, та Г.М. Морозовська

Анотація. У цій роботі встановлено зв'язок між симетрією кристалічної структури, точковими дефектами та можливою появою сегнетоелектричної поляризації в наночастинках HfO_{2-y} . Примітно, що аналіз за допомогою дифракції X-променів та електронного парамагнітного резонансу виявили утворення сегнетоелектричної орторомбічної фази в наночастинках HfO_{2-y} з дефіцитом кисню як без домішок, так і у наночастинках, легуваних рідкоземельним елементом ітрієм. Розрахунки за допомогою теорії функціонала густини (DFT) показали, що малі наночастинки HfO_2 можуть стати полярними, особливо за наявності домішкових атомів та/або кисневих вакансій. Щоб пояснити експериментальні результати, ми модифікували ефективну модель Ландау–Гінзбурга–Девоншира (LGD) за допомогою підходу параметризації, зосередившись на коефіцієнтах розкладу у вільній енергії, пов'язаних із полярним та антиполярним упорядкуваннями, що узгоджується з розрахунками DFT. Ефективна модель LGD може бути корисною для розробки нового покоління кремній-сумісних сегнетоелектричних наноматеріалів на основі $\text{Hf}_x\text{Zr}_{1-x}\text{O}_{2-y}$.

Ключові слова: наночастинки, оксид гафнію, кисневі вакансії, легування рідкоземельними елементами, сегнетоелектрична полярна фаза, кремній-сумісні сегнетоелектричні наноматеріали.